Crystal-melt interfacial free energies in hcp metals: A molecular dynamics study of Mg

D. Y. Sun,[1] M. I. Mendelev,[2] C. A. Becker,[3] K. Kudin,[4] Tomorr Haxhimali,[5] M. Asta,[6] J. J. Hoyt,[7] A. Karma,[5] and D. J. Srolovitz[4]

[1]*Department of Physics, East China Normal University, Shanghai-200062, China*

[2]*Materials and Engineering Physics Program, Ames Laboratory, Ames, Iowa, USA*

[3]*Department of Materials Science and Engineering, Northwestern University, Evanston, Illinois 60208, USA*

[4]*Princeton Materials Institute, Department of Mechanical and Aerospace Engineering, Princeton University, Princeton, New Jersey 08544, USA*

[5]*Department of Physics, Northeastern University, Boston, Massachusetts, USA*

[6]*Department of Chemical Engineering and Materials Science, Center for Computational Science and Engineering, University of California, Davis, Davis, California 95616, USA*

[7]*Sandia National Laboratories, MS 1411, Albuquerque, New Mexico 87185, USA*

(Received 14 October 2005; published 31 January 2006)

Crystal-melt interfacial free energies (γ) are computed for hcp Mg by employing equilibrium molecular-dynamics (MD) simulations and the capillary-fluctuation method (CFM). This work makes use of a newly developed embedded-atom-method (EAM) interatomic potential for Mg fit to crystal, liquid, and melting properties. We describe how the CFM, which has previously been applied to cubic systems only, can be generalized for studies of hcp metals by employing a parametrization for the orientation dependence of γ in terms of hexagonal harmonics. The method is applied in the calculation of the Turnbull coefficient (α) and crystalline anisotropies of γ. We obtain a value of $\alpha=0.48$, with interfacial free energies for different high-symmetry orientations differing by approximately 1%. These results are compared to those obtained in previous MD-CFM studies for cubic EAM metals as well as experimental studies of solid-liquid interfaces in hcp alloys. In addition, the implications of our results for the prediction of dendrite growth directions in hcp metals are discussed.

DOI: 10.1103/PhysRevB.73.024116 PACS number(s): 68.08.−p, 64.70.Dv, 81.30.Fb

I. INTRODUCTION

The excess free energy of the crystal-melt interface (γ) and its dependence on crystalline orientation ($\hat{n}$) are critical factors influencing nucleation rates, phase selection, and microstructural morphology in the growth of a crystal from its melt. In particular, dendrite growth directions and growth rates are known to be extremely sensitive to the weak anisotropy of γ in metallic systems.[1] Due to the difficulties inherent in performing direct experimental measurements of the properties of solid-liquid interfaces, to date much of the most detailed information concerning the magnitude and anisotropy of γ has been derived from molecular-dynamics (MD) simulations.[2–15] Highly precise MD-based calculations of γ have been facilitated by the development of two complementary techniques: the so-called cleaving method, first proposed by Broughton and Gilmer[2] and subsequently extended by Davidchack and Laird,[3–5] and the capillary-fluctuation method (CFM).[6,10] The CFM has been used to calculate anisotropic values of γ for a variety of elemental fcc and bcc metals,[6–10,12,13] as well as one alloy system,[15] all modeled with interatomic potentials of the embedded-atom-method (EAM) form.[16] In addition, the cleaving method has been extensively applied to the study of crystal-melt interfacial free energies in a variety of model systems including hard spheres[3,14] and repulsive power-law potentials.[5] Both the CFM and cleaving methods were applied to the calculation of γ and its anisotropy for the Lennard-Jones system,[2,4,11] where good agreement was demonstrated between results obtained from these two independent methods.

The extensive body of simulation work devoted to the study of crystal-melt interfaces has yielded interesting correlations between the magnitudes and anisotropies of γ and the atomic structures of the bulk solid and liquid phases. For example, the simulation results for the magnitude of γ are found to obey well the scaling relation originally proposed by Turnbull:[17] $\gamma n^{-2/3}=\alpha L$, where n is the solid atomic density and L is the latent heat (per atom). For fcc EAM metals, MD-CFM calculations give an average value for the Turnbull coefficient of $\alpha=0.55$,[13] in close correspondence with the value of $\alpha=0.51$ for hard spheres.[18] For bcc EAM metals the average Turnbull coefficient calculated by MD simulations is lower, with $\alpha=0.29$.[9] This trend towards lower values of α for bcc relative to fcc systems was also found in recent MD calculations for repulsive power-law potentials.[5] The lower values of α obtained by MD calculations for bcc relative to fcc solids are consistent with the trend previously inferred from experimental and simulation-based nucleation studies (e.g., Refs. 19–26) and from a polytetrahedral model for the (negative) excess configurational entropy of crystal-melt interfaces.[27–29] Another important feature of the simulation results concerns the effect of crystal structure on γ anisotropies. For fcc-based systems, MD calculations yield anisotropies between {110}, {111}, and {100} interface orientations in the following ranges: $(\gamma_{100}-\gamma_{110})/2\gamma_0=0.8-2.5\%$ and $(\gamma_{100}-\gamma_{111})/2\gamma_0=1.8-3.2\%$,[9] where γ_0 is the orientation-averaged value of γ. The magnitudes of these calculated anisotropies are consistent with recent values for fcc Al-based alloys measured experimentally.[30–32] Recent

calculations for bcc-based systems yield slightly smaller anisotropies, particularly for $\gamma_{111}/\gamma_{100}$.[9] A trend towards lower anisotropies in bcc relative to fcc systems is also found in the measurements reported for transparent organic systems succinonitrile (bcc) and pivalic acid (fcc).[33,34] Recently, through consideration of two different potential models for Al, a trend towards increasing values of γ with increasing icosahedral short-range order in the liquid phase was also demonstrated.[12]

To date all simulation-based studies of crystal-melt interfaces have focused on systems with cubic (fcc or bcc) crystal structures. The present work involves the generalization of the CFM method in the calculation of crystal-melt interfacial free energies for hcp metals. We describe how the CFM can be readily applied to the calculation of γ and its anisotropy for hcp systems by employing a parametrization of $\gamma(\hat{n})$ in terms of hexagonal harmonics. The approach demonstrated in this work allows the analysis of the correlations between crystal structure and γ, as summarized above, to be extended in the consideration of the most commonly occurring noncubic crystal structure for elemental metals and alloy solid solutions, namely, hcp.

In this initial application of the CFM to hcp systems, we focus on elemental Mg. This choice was motivated by the growing interest in Mg-based alloys as light-weight structural materials, and the associated relevance of the solidification microstructures resulting from their casting. In this study we make use of a newly developed EAM potential for Mg fit to experimentally measured and first-principles-calculated properties for both crystalline and liquid phases, as well as the melting temperature. This work thus extends the previous work by Liu *et al.*,[35] who also generated an EAM Mg potential by fitting to both liquid and crystal properties. Relative to this earlier work, the potential developed here is found to yield improved predictions for the equilibrium melting properties and high-temperature phase stability, as will be discussed below.

In the following section, the details of the application of the CFM method to hcp systems are described, and expressions are given for the stiffnesses of high-symmetry interface orientations, expressed in terms of hexagonal harmonics. Details of the Mg interatomic-potential development are then described, and results for benchmark structural and energetic properties in solid and liquid phases presented. The results for the crystal-melt interfacial free-energy are presented in Sec. IV and discussed in Sec. V relative to previous calculations and experimental findings in hcp alloys. The main conclusions are summarized in Sec. VI.

II. CAPILLARY FLUCTUATION METHOD

In the CFM, crystal-melt interfacial free energies are derived through an analysis of equilibrium interface-height fluctuations obtained from MD simulations for coexisting solid-liquid systems. The method is based on the well-known relationship between the static height-fluctuation spectrum of a molecularly rough interface and its stiffness:

$$\langle |A(k)|^2 \rangle = \frac{k_B T_M}{bW(\gamma + \gamma'')k^2}, \tag{1}$$

where $A(k)$ is the Fourier amplitude of the interface height fluctuation with wave number k, b, and W are the dimensions of the interface plane, k_B is Boltzmann's constant, and T_M is the melting temperature. In Eq. (1), $\gamma+\gamma''$ denotes the interface stiffness, where γ'' is the second derivative of γ with respect to the orientation of the interface normal ($\hat{n}$).

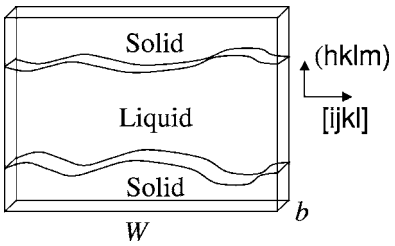

FIG. 1. Schematic illustration of the geometry of the simulation cells employed in CFM calculations of interfacial free energies.

In the CFM, interface fluctuations are measured from equilibrium MD simulations which typically make use of quasi-two-dimensional cell geometries, as illustrated schematically in Fig. 1. The area of the plane of the ribbonlike interface is $b \times W$, where b and W are the short and long dimensions, respectively. In such simulations, the instantaneous position of the crystal-melt interface is derived through the use of a local structural order parameter;[6,10] in the present work we make use of the crystalline-order parameter (Φ) introduced by Hoyt *et al.*[6]

$$\Phi = \frac{1}{12}\sum_i |\vec{r}_i - \vec{r}_{\text{ideal}}|^2, \tag{2}$$

where the sum is over the twelve nearest neighbors (for fcc and hcp crystals) of a given atom, $\vec{r}_i$ is the position of neighboring atom i, and $\vec{r}_{\text{ideal}}$ is the ideal position of atom i in the ideal crystal structure. For a given MD snapshot, the order parameter is computed for each atom in the simulation box, and the interface location is identified as the position where the average value of Φ has a magnitude half way between those in the crystal and melt phases. The amplitudes $A(k)$ are obtained through a real-space Fourier transform of the interface location along the long periodic dimension parallel to the boundary plane. This is performed for each snapshot and the results are time averaged to obtain $\langle |A(k)|^2 \rangle$. A fit of $\langle |A(k)|^2 \rangle$, versus $1/k^2$ is then used to derive values for the stiffness $\gamma+\gamma''$.

Once the stiffnesses have been calculated for several interface orientations, the orientation-averaged interfacial free energy (γ_0) and the associated crystalline anisotropies are derived by employing an analytical parametrization for the dependence of γ on interface normal $\hat{n}$. For the cubic systems studied to date this parametrization takes the form of an expansion of $\gamma(\hat{n})$ in terms of cubic harmonics, i.e., linear combinations of spherical harmonics which are compatible with the cubic symmetry of the crystal. Specifically, the following three-parameter expansion (e.g., Ref. 15) has proven sufficient to model the orientation dependencies of γ and stiffness derived from MD simulations for a variety of fcc and bcc systems:

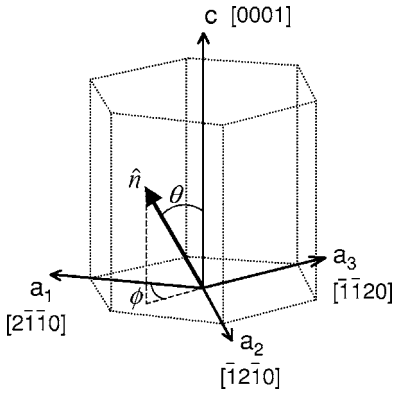

FIG. 2. Coordinate system employed in the current work. θ and ϕ are spherical-coordinate angles used to define the orientation of the normal ($\hat{n}$) to the crystal-melt interface.

$$\gamma(\hat{n}) = \gamma_0\left[1 + \epsilon_1\left(\sum_{i=1}^{3} n_i^4 - \frac{3}{5}\right) + \epsilon_2\left(3\sum_{i=1}^{3} n_i^4 + 66 n_1^2 n_2^2 n_3^2 - \frac{17}{7}\right)\right], \quad (3)$$

where ϵ_1 and ϵ_2 denote the magnitudes of the fourfold and sixfold anisotropies, respectively. With the use of Eq. (3), application of the CFM to cubic systems requires that a minimum of three stiffness values be derived for different interface orientations by MD, from which γ_0 and the two anisotropy coefficients can be obtained. These in turn provide a full parametrization of $\gamma(\hat{n})$.

In the application of the CFM to hcp systems, the procedure summarized above can be readily employed in the calculation of $\gamma(\hat{n})$, provided Eq. (3) is replaced with the form appropriate for an hcp crystal structure. In this work, we accordingly make use of a parametrization of $\gamma(\hat{n})$ in terms of hexagonal harmonics. Specifically, we make use of the fact that the symmetry of $\gamma(\hat{n})$ is governed by the point group isogonal with the space group of the crystal structure (e.g., Ref. 36). For the hcp structure, this point group is $6/mmm$ (D_{6h}), and accordingly the orientation dependence of $\gamma(\hat{n})$ can be written as follows:[37]

$$\gamma(\theta,\phi) = \gamma_0[1 + \epsilon_{20} y_{20}(\theta,\phi) + \epsilon_{40} y_{40}(\theta,\phi) + \epsilon_{60} y_{60}(\theta,\phi) + \epsilon_{66} y_{66}(\theta,\phi) + \cdots], \quad (4)$$

where the interface normal is specified by the spherical-coordinate angles θ and ϕ. The definition of these angles is illustrated in Fig. 2 where the choice of coordinate system adopted in this work is also specified with reference to high-symmetry directions in the hcp structure. The functions $y_{lm}(\theta,\phi)$ in Eq. (4) represent normalized real spherical harmonics taking the following form:

$$y_{20}(\theta,\phi) = \sqrt{\frac{5}{16\pi}}[3\cos^2(\theta) - 1],$$

$$y_{40}(\theta,\phi) = \frac{3}{16\sqrt{\pi}}[35\cos^4(\theta) - 30\cos^2(\theta) + 3],$$

$$y_{60}(\theta,\phi) = \frac{\sqrt{13}}{32\sqrt{\pi}}[231\cos^6(\theta) - 315\cos^4(\theta) + 105\cos^2(\theta) - 5],$$

$$y_{66}(\theta,\phi) = \frac{\sqrt{6006}}{64\sqrt{\pi}}[1 - \cos^2(\theta)]^3\cos(6\phi). \quad (5)$$

In Eq. (4), we have included terms in the expansion up to $l = 6$, which include the lowest-order spherical harmonic (namely, y_{66}) parametrizing anisotropy of γ within the (0001) basal plane. As will be shown below, the y_{66} term is found to be crucial for obtaining a good fit to the MD stiffness results for hcp Mg.

In applying the CFM to hcp Mg, MD simulations have been performed for a total of five interface orientations derived from the three high-symmetry interface planes illustrated in Fig. 3. The orientations are specified following the notation introduced in Fig. 1 where ($hklm$) gives the Miller indices of the interface plane (using the standard four-index system for a hexagonal crystal), and $[ijkl]$ gives the crystallographic direction within the interface plane along which height fluctuations are calculated by MD. Table I lists the interface orientations considered in the present study and provides expressions for the stiffness in terms of the anisotropy parameters introduced in Eq. (5). Also listed in Table I are the cell dimensions b and W, parallel to the solid-liquid interface plane, employed for each simulation cell. The remaining periodic dimension, perpendicular to the interface, was chosen as roughly $2W$, giving a total number of atoms in each cell of approximately 60 000. For each orientation, the coexisting solid-liquid system was equilibrated as follows.

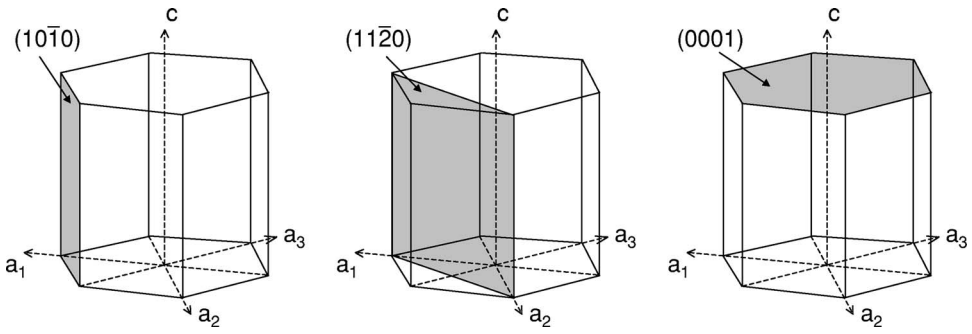

FIG. 3. Illustration of the high-symmetry planes investigated in the MD simulations of crystal-melt interfaces for hcp Mg.

TABLE I. Expressions for interface stiffness and simulation-cell dimensions for the interface orientations considered in this work.

$(hklm)$	$[ijkl]$	$(\gamma+\gamma')/\gamma_0$	b (nm)	W (nm)
(0001)	$[10\bar{1}0]$	$1-\sqrt{5/\pi}\,\epsilon_{20}-\frac{27}{2}\sqrt{1/\pi}\,\epsilon_{40}-10\sqrt{13/\pi}\,\epsilon_{60}$	2.276	18.020
$(10\bar{1}0)$	[0001]	$1+\frac{5}{4}\sqrt{5/\pi}\,\epsilon_{20}-\frac{171}{16}\sqrt{1/\pi}\,\epsilon_{40}+\frac{205}{32}\sqrt{13/\pi}\,\epsilon_{60}+\frac{5}{64}\sqrt{6006/\pi}\,\epsilon_{66}$	1.951	18.078
$(10\bar{1}0)$	$[\bar{1}2\bar{1}0]$	$1-\frac{1}{4}\sqrt{5/\pi}\,\epsilon_{20}+\frac{9}{16}\sqrt{1/\pi}\,\epsilon_{40}-\frac{5}{32}\sqrt{13/\pi}\,\epsilon_{60}+\frac{35}{64}\sqrt{6006/\pi}\,\epsilon_{66}$	2.127	19.507
$(11\bar{2}0)$	[0001]	$1+\frac{5}{4}\sqrt{5/\pi}\,\epsilon_{20}-\frac{171}{16}\sqrt{1/\pi}\,\epsilon_{40}+\frac{305}{32}\sqrt{13/\pi}\,\epsilon_{60}-\frac{5}{64}\sqrt{6006/\pi}\,\epsilon_{66}$	2.253	18.078
$(11\bar{2}0)$	$[\bar{1}100]$	$1-\frac{1}{4}\sqrt{5/\pi}\,\epsilon_{20}+\frac{9}{16}\sqrt{1/\pi}\,\epsilon_{40}-\frac{5}{32}\sqrt{13/\pi}\,\epsilon_{60}-\frac{35}{64}\sqrt{6006/\pi}\,\epsilon_{66}$	2.127	18.020

In the initial step, the lattice constants of the solid and the atomic density of the liquid are determined at the melting point. This information is then used to determine the periodic lengths of the solid-liquid interface cells; the dimensions parallel to the interface are fixed by the zero-pressure lattice constants of the crystal while the periodic length normal to the solid-liquid interface is set to give a total cell volume corresponding to a sample with equal volume fractions solid and liquid. The initial sample is constructed with atoms in bulk crystal positions and subsequently half of the atoms are held fixed in high-temperature MD simulations (at 1.5 times the melting temperature T_M) used to melt the other half of the sample. This process lasts roughly 10 ps, after which an additional MD simulation of comparable length is performed with the temperature set equal to T_M and the atoms in the crystalline half of the sample remaining fixed. Subsequently, all of the atoms are allowed to be dynamic in a canonical ensemble (NVT) MD simulation at the melting temperature lasting roughly 20 ps. Next, the simulations are equilibrated in a microcanonical ensemble (NVE). The final statistics for interface fluctuations are conducted in NVE simulations lasting a total of approximately 150 ps, with interface positions sampled once every 0.02 ps. For each snapshot the interface height profile was determined by averaging the crystalline order parameter, defined in Eq. (2), over cube volumes with an edge length equal to 1/12 the long periodic dimension parallel to the interface. Fourier transforms of the resulting heights were then averaged over snapshots to derive $\langle|A(k)|^2\rangle$. In all of the MD simulations a time step of 0.002 ps was employed. The details of the interatomic potential employed in this work are given in the following section.

III. INTERATOMIC POTENTIAL FOR MG

Quantitative studies of crystal-melt interfacial free energies require as a prerequisite interatomic potentials which accurately model the bulk thermodynamic properties of the relevant crystal and liquid phases, along with the equilibrium melting properties including melting temperature and latent heat. Two classes of interatomic potentials have been employed in previous work to model the bulk thermodynamic properties of Mg, namely, density-dependent pair potentials[38,39] and many-body embedded-atom-method potentials.[35] While pair potentials have been successfully applied in calculations of the bulk structural and thermodynamic properties, as well as the pressure-temperature phase diagram for Mg,[38,39] EAM potentials are preferred in the present work which involves simulations of coexisting solid and liquid phases with different densities; the application of density-dependent pair potentials in simulations for inhomogeneous systems (such as solid-liquid interface cells) is conceptually far less straightforward than the application of EAM potentials which incorporate in a natural way variations in interatomic interactions arising from local changes in electron density (e.g., Ref. 40). For the present work we thus focus on the application of EAM potentials in the modeling of solid-liquid interfaces in elemental Mg.

A highly developed EAM potential for Mg was published previously by Liu *et al.*;[35] in the following we refer to this as the "LAEM" potential after the initials of the authors of Ref. 35. The LAEM potential was developed using the so-called force-matching method.[41] In this approach, model liquid configurations are generated and the total forces on each atom are obtained from first-principles calculations. The potential parameters are then fit to these data together with such crystal properties as the lattice parameters, cohesive and vacancy-formation energies, the elastic constants and other related properties (see Ref. 41 for details).

Table II compares crystalline and liquid Mg properties predicted by the LAEM potential with values obtained either from first-principles calculations performed in the course of this work, or from experimental measurements. For the zero-temperature properties, the lattice constants, elastic and cohesive properties predicted by the LAEM potential for hcp and fcc Mg are in good agreement with the current first-principles calculations, while predictions for the bcc lattice show significant deviations. The unrelaxed vacancy-formation energy predicted by the LAEM potential is slightly larger than that derived from first principles.

In addition to the vacancy formation energy, a calculation of the vacancy migration energy was also undertaken in the current work. This property was derived from MD simulations in which one vacancy was introduced by removing an atom from an hcp simulation cell consisting of 1848 atoms. After equilibration, NVT MD simulations lasting 4 ns (as above, the time step for the MD integrations was 0.002 ps) were conducted to determine the diffusivity (D) from the mean-square displacement (Δr^2) as a function of time (t) via the Einstein relation $D=\langle\Delta r^2\rangle/6t$. Such simulations were undertaken at several temperatures and the resulting values of D are shown on an Arrhenius plot in Fig. 4. Since the vacancy concentration was constant the temperature dependence of D is determined solely by the vacancy migration energy listed in Table II. The sum of the calculated vacancy formation energy and the migration energy gives the activa-

TABLE II. Physical properties of Mg calculated by the LAEM and current EAM potentials.

Property	Target value	LAEM potential	New potential[a]
a (hcp) (Å)	3.186[b]	3.206	**3.184**
c/a (hcp)	1.622[b]	1.623	**1.628**
E_{coh} (hcp) (eV/atom)	1.510[c]	1.517	**1.529**
C_{11} (GPa)	63.5[c]	63.4	**69.6**
C_{12} (GPa)	26.0[c]	24.8	**25.3**
C_{44} (GPa)	18.4[c]	18.1	**12.8**
C_{13} (GPa)	21.7[c]	22.0	**16.0**
C_{33} (GPa)	66.5[c]	67.3	**69.5**
a (fcc) (Å)	4.496[b]	4.519	**4.495**
$\Delta E_{fcc\rightarrow hcp}$ (eV/atom)	0.013[b]	0.013	**0.012**
a (bcc) (Å)	3.568[b]	3.576	**3.562**
$\Delta E_{bcc\rightarrow hcp}$ (eV/atom)	0.029[b]	0.016	**0.014**
E_f^v (unrelaxed, hcp) (eV/atom)	0.82[b]	0.88	**0.90**
E_f^v (relaxed, hcp) (eV/atom)		0.88	0.88
E_f^m (hcp) (eV/atom)		0.43	0.64
E_D (hcp) (eV/atom)	1.40[d]	1.31	1.52
R_F (eV/Å)	0.000	0.097[e]	**0.141**
n (liquid at T=923 K) (atom/Å^3)	0.039[f]	0.0374	**0.0389**
T_{melt} (hcp) (K)	923[g]	745±4	**914±3**
L (hcp) at T_{melt} (eV/atom)	0.088[g]	0.073	**0.098**
$\Delta\Omega_{melt}$ (hcp) at T_{melt} (%)	4.1[h]	4.4	**6.0**
T_{melt} (bcc) (K)	900[i]	766±5	905±7
L (bcc) at T_{melt} (eV/atom)		0.064	0.081
$r\Delta\Omega_{melt}$ (bcc) at T_{melt} (%)		4.5	5.1

[a]The properties used in the fitting procedure are printed in bold.
[b]First-principles calculations performed as part of this work.
[c]Input data taken from Ref. 35.
[d]Reference 42.
[e]This value was obtained using the same liquid configuration as in the development of the new potential.
[f]Reference 43.
[g]Reference 44.
[h]Reference 45.
[i]Value set to ensure a lower predicted melting point for bcc relative to hcp (see text for a detailed explanation).

tion energy for self diffusion, which is compared with experimental values[42] in Table II. Note that in the case of hcp Mg, experimental measurements find that the diffusivity is anisotropic although the activation energy is almost isotropic (within the accuracy of the measurements[42]). The LAEM potential is found to yield good agreement with measurements for the activation energy of self diffusion in the hcp lattice.

Of direct relevance for the present work are the predictions for liquid structure and melting properties. Considering first the liquid structure, Fig. 5 gives a comparison of the structure factor calculated (at zero pressure) with the LAEM potential and that derived from experimental data[46] at T =953 K. Except for the region near the first minimum, the agreement between the two curves is nearly perfect. It is worth noting that although the LAEM liquid structure factor is in excellent agreement with experiment, this potential predicts an atomic density of 37.2 nm^{-3} at 953 K which is roughly 3% smaller than the reported measured value of 38.3 nm^{-3}.

We turn now to the predictions of melting properties, focusing specifically on the melting temperature. For the hcp structure the melting temperature originally reported by Liu *et al.*[35] was checked in the current work through an implementation of the so-called coexistence approach,[47] as detailed in Ref. 48. Similar to the result originally reported by Liu *et al.*, the LAEM potential is shown in Table II to underestimate the hcp melting point by nearly 180 K. Of more serious concern for the current work was the observation of a higher melting point predicted for the bcc solid. In initial LAEM-MD simulations performed in this work, it was noted that the bcc crystal was found to be stable up to temperatures comparable to the hcp melting temperature (fcc by comparison melted at relatively low temperatures). This observation motivated more detailed coexistence simulations to calculate

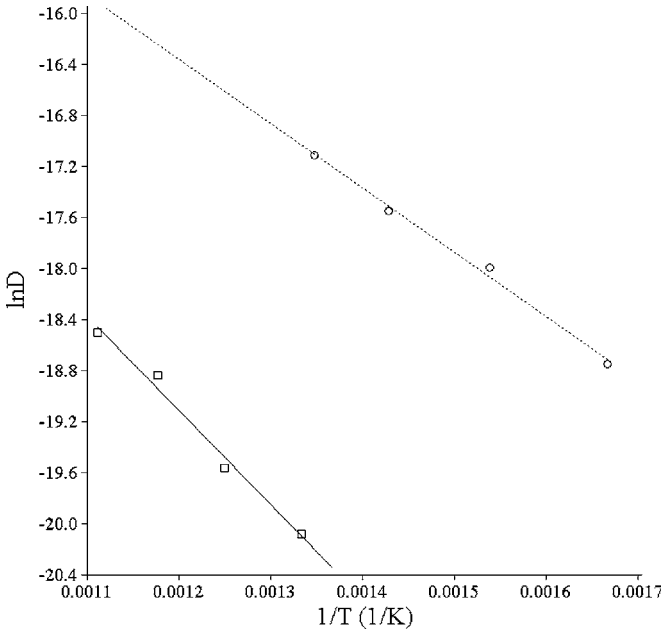

FIG. 4. The temperature dependence of the diffusivity calculated under the condition of a fixed vacancy concentration (see text). The calculated results correspond to MD simulations based on the LAEM potential (circles) and the potential developed in the present work (squares).

the bcc melting temperature listed in Table II. The resulting bcc melting temperature is seen to be higher than that for hcp by roughly 20 K. These results thus indicate that the hcp phase is predicted by the LAEM potential to transform to bcc prior to melting. The equilibrium temperature for the hcp to bcc transition ($T^{\mathrm{hcp}\rightarrow\mathrm{bcc}}$) was calculated employing thermodynamic integrations based on the Gibbs-Helmholtz equation in the form

$$\int_{T^{\mathrm{hcp}\rightarrow\mathrm{bcc}}}^{T_m^{\mathrm{bcc}}} \frac{\Delta H^{\mathrm{hcp}\rightarrow\mathrm{bcc}}}{T^2} dT + \int_{T_m^{\mathrm{bcc}}}^{T_m^{\mathrm{hcp}}} \frac{\Delta H_m^{\mathrm{hcp}}}{T^2} dT = 0, \qquad (6)$$

where $\Delta H^{\mathrm{hcp}\rightarrow\mathrm{bcc}}(T)$ is the hcp-bcc enthalpy difference and $\Delta H_m^{\mathrm{hcp}}$ is the enthalpy difference between the hcp crystal and the liquid. The temperature dependencies of these enthalpy differences were obtained by zero-pressure MD simulations. When the resulting values were used in Eq. (6), a value of $T^{\mathrm{hcp}\rightarrow\mathrm{bcc}}=645\pm40$ K was derived. The LAEM potential thus predicts that the bcc phase is stable over a temperature range of roughly 120 K prior to melting. While an hcp$\rightarrow$bcc transition with increasing temperature has been predicted for Mg at high pressures,[39] it is inconsistent with the experimental phase diagram at ambient pressure. The presence of a stable bcc phase at temperatures above the hcp melting point represents a cause for concern in the application of the LAEM potential to studies of hcp crystal-melt interfaces; in principle the bcc phase may form in simulations of hcp crystal-melt interfaces, particularly when considering interface orientations for which the hcp-bcc interfacial energy is relatively low. The unexpected high-temperature stability of the bcc phase obtained with LAEM potential motivated an effort in this work to develop an EAM potential for Mg with improved melting temperatures and finite-temperature phase stability, as described in the remainder of this section.

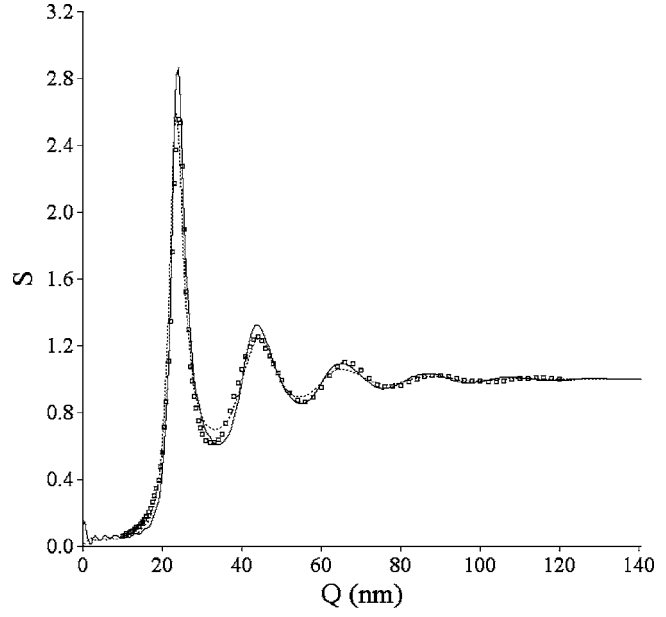

FIG. 5. The structure factor of liquid Mg at $T=953$ K obtained from x-ray diffraction experiments (Ref. 46) and calculated by MD simulations based on the LAEM (dotted line) and currently developed (solid line) EAM potentials.

In developing a new EAM potential for Mg, we adopted an approach similar to that employed in previous work for Fe in Ref. 48. As in the LAEM work, the current potential development is based on the use of the force-matching method, but it additionally includes an implementation of the approach for fitting equilibrium melting temperatures proposed by Sturgeon and Laird.[49] This procedure allowed us to ensure that the predicted melting temperature for hcp was higher than that for bcc at ambient pressure.

To construct the new EAM potential we first generated a small liquid configuration consisting of 128 atoms. The forces on each atom in this configuration were computed from first principles using the PWSCF code[51] employing norm-conserving pseudopotentials and the generalized-gradient approximation of Perdew *et al.*[52] Convergence of the forces with respect to the sampling of the Brillouin zone was carefully checked and made use of a conventional broadening of the electronic levels. In the development of the Mg potential we used, as one of the properties in the fit, the following quantity which represents a criterion for fitting the resulting first-principles forces:

$$R_F = \sqrt{\frac{1}{3N}\sum_{i=1}^{N}\left[(F_{ix}-F_{ix}^{fp})^2+(F_{iy}-F_{iy}^{fp})^2+(F_{iz}-F_{iz}^{fp})^2\right]}, \qquad (7)$$

where $F_{i\alpha}$ and $F_{i\alpha}^{fp}$ are the α components of the forces on atom i calculated with the EAM potential and from first principles, respectively. In order to be self consistent, we also used in the fitting values for the hcp, fcc, and bcc lattice

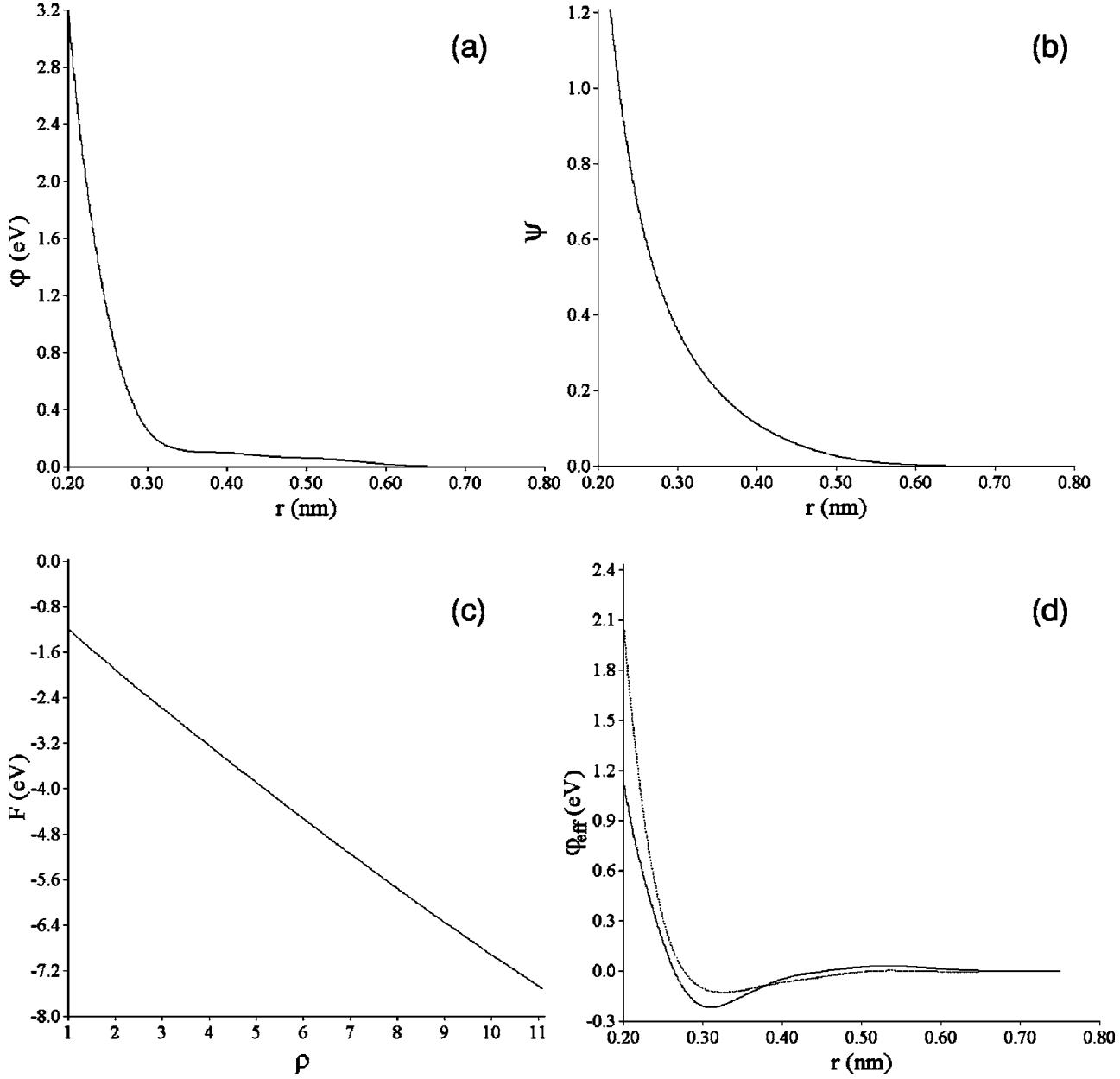

FIG. 6. The pairwise (a), density (b), and embedding-energy (c) functions of the currently developed EAM potential for Mg. In (d) the effective pair potentials calculated from the LAEM (dotted line) and new (solid line) potentials are plotted.

parameters, energy differences, and unrelaxed vacancy formation energy as a function of the hcp atomic volume (with fixed c/a ratio), all derived from first-principles calculations employing the same method. These data, together with the universal binding-energy relation[50] and elastic constants, were used to produce the first iteration of the potential. Subsequently, the potential parameters were re-optimized to obtain the melting-point data and the correct liquid density at the T_M. The procedure of Sturgeon and Laird[49] was used to fit the hcp melting temperature to the experimental value; to ensure a lower value for the bcc melting temperature, a value of 900 K was used in the fitting of this quantity. Due to uncertainties in the actual value of the bcc melting point, the equation for the bcc melting temperature was given half the weight in the fitting relative to that for hcp. The resulting potential parameters derived from this procedure are given in the Appendix. The pair potential $[\phi(r)]$, electron density $[\psi(r)]$, embedding function $[F(\rho)]$ and effective pair potential (ϕ^{eff}) are plotted in Figs. 6(a)–6(d). The effective pair potential is defined as follows:[40]

$$\phi^{\text{eff}}(r) = \phi(r) + 2F'(\rho_0)\psi(r), \tag{8}$$

where $F'(\rho_0)$ denotes the derivative of the embedding function evaluated at the electron density (ρ_0) at an atomic site in an hcp lattice with the equilibrium zero-temperature lattice constants. In Fig. 6(d), ϕ^{eff} derived from the LAEM and new potentials are plotted for comparison. The new potential has a longer range and deeper minimum than the LAEM potential. It is also softer at short distances and possesses a region

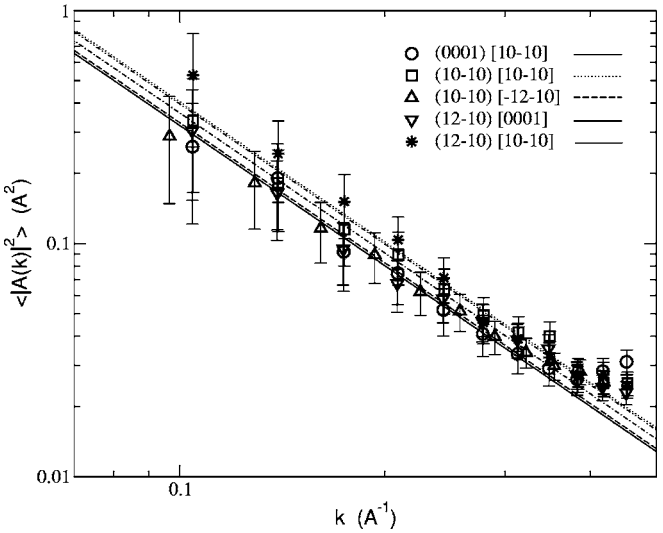

FIG. 7. Log-log plot of the fluctuation spectra $\langle|A(k)|^2\rangle$ versus wave number (k). The symbols are MD-calculated data for five interface orientation, with error bars denoting estimated standard statistical uncertainties. The lines represent fits of the MD data to the theoretical $1/k^2$ relation.

of repulsive interactions at larger interatomic separations.

The properties predicted by the new EAM Mg potential are given in the fourth column of Table II. The new potential is seen to provide slightly poorer values for the crystal properties (with the exception of thermal expansion). The liquid structure factor predicted by the new potential is shown in Fig. 5 and, except for the region near the first minimum, it is seen to be in slightly poorer agreement with experiment than the LAEM potential. However, given that the LAEM melting point is significantly different from experiment, the slightly better agreement with the measured liquid structure factor may be somewhat fortuitous. The most important feature of the new potential is that it provides an hcp melting temperature in very reasonable agreement with experiment and correctly reproduces the stability of hcp relative to bcc up to the melting point.

IV. RESULTS

Figure 7 plots the MD-calculated fluctuation spectra for the five interface orientations listed in Table I. The results are plotted on a log-log plot as $\langle|A(k)|^2\rangle$ versus k, and the solid lines indicate best fits to the theoretical $1/k^2$ dependence given in Eq. (1). The error bars in Fig. 7 represent estimates of the standard statistical errors, derived from measured correlation times, following the procedure described in Ref. 7. Similar to the results obtained in previous applications of the CFM to EAM metals, the theoretical dependence ($\langle|A(k)|^2\rangle \propto 1/k^2$) is found to be obeyed well for fluctuation wavelengths $\lambda=2\pi/k$ larger than about 1.5 nm (i.e., $k\lesssim 0.4$ Å^{-1}), while systematic deviations are obtained at higher k. The values of the interface stiffnesses given in Table III were derived by performing a least-squares fit of Eq. (1) to the MD fluctuation amplitudes (weighted by the error bars) for wave numbers in the range of $k=0.04-0.4$ Å^{-1}. To determine the average value and crystalline anisotropy of $\gamma(\hat{n})$ from this data, the parameters in Eq. (4) are derived by fitting the stiffness data in Table III to the expressions given in Table I.

TABLE III. MD-calculated (second column) and fitted (third column) fluctuation amplitudes for hcp Mg for the five interface orientations considered in this work. Error bars in the second column denote estimated standard statistical uncertainties.

Orientation	$\gamma+\gamma''$ (mJ/m^2)	Fit (mJ/m^2)
$(0001)[10\bar{1}0]$	95.9±3.3	92.9
$(10\bar{1}0)[0001]$	88.7±2.8	87.0
$(10\bar{1}0)[\bar{1}2\bar{1}0]$	94.1±2.2	96.5
$(11\bar{2}0)[0001]$	85.2±3.7	85.4
$(11\bar{2}0)[\bar{1}100]$	82.7±2.3	84.8

From the analytical expressions given in Table I, it can be seen that the ϵ_{66} parameter determines the difference between the traces of the stiffness in the $(11\bar{2}0)$ and $(10\bar{1}0)$ planes:

$$\frac{80}{64}\sqrt{\frac{6006}{\pi}}\gamma_0\epsilon_{66} = [\tilde{\gamma}_{(10\bar{1}0)[0001]} + \tilde{\gamma}_{(10\bar{1}0)[\bar{1}2\bar{1}0]}] - [\tilde{\gamma}_{(11\bar{2}0)[0001]} + \tilde{\gamma}_{(11\bar{2}0)[\bar{1}100]}], \quad (9)$$

where we have used the symbol $\tilde{\gamma}\equiv\gamma+\gamma''$ to denote interface stiffness. From the stiffness values listed in Table III we obtain a value of 14.9±5.7 for the right-hand side of Eq. (9). These results establish that the ϵ_{66} parameter is required in the modeling of the MD-calculated stiffnesses in order to reproduce the statistically significant anisotropy of the stiff-

TABLE IV. Interfacial free energies and associated crystalline anisotropies derived for hcp Mg. Error bars represent estimated standard statistical uncertainties.

γ_0	ϵ_{20}	ϵ_{66}	α	$\frac{\gamma_{11\bar{2}0}-\gamma_{10\bar{1}0}}{2\gamma_0}$	$\frac{\gamma_{11\bar{2}0}-\gamma_{0001}}{2\gamma_0}$
(mJ/m^2)	(%)	(%)		(%)	(%)
89.9±1.5	−2.6±1.5	0.3±0.1	0.48±0.01	0.18±0.08	1.2±0.7

ness trace for $\hat{n}$ within the basal plane. In the fitting of the MD data, we thus attempted different fits, including from Eq. (4) the parameters γ_0, ϵ_{66}, and various combinations of the anisotropy parameters ϵ_{l0}, for $l=2,4$, and 6. Of these fits, the only one that yielded statistically significant values for all of the coefficients included γ_0, ϵ_{20}, and ϵ_{66}.

The resulting fit, involving two anisotropy parameters, is shown in Table III to reproduce the five calculated stiffnesses to within the estimated statistical uncertainties of the MD data. The fitted values of the orientation-averaged interfacial free energy (γ_0) and crystalline-anisotropy parameters (ϵ_{20} and ϵ_{66}) are given in Table IV, along with the associated values for the Turnbull coefficient (α), and the differences in interfacial free energies between the three high-symmetry orientations $\hat{n}=[0001]$, $[10\bar{1}0]$, and $[11\bar{2}0]$.

V. DISCUSSION

The value of the Turnbull coefficient for hcp Mg quoted in Table IV can be compared with values derived in previous CFM studies of fcc and bcc EAM metals.[8–10,13] The fcc values range from 0.46 to 0.62, while for bcc the values vary between 0.27 and 0.36. The present value of $\alpha=0.48$ for hcp Mg is found to lie within the range previously derived for fcc metals, while it is larger than any of the values obtained for bcc EAM systems. These results suggest that the higher values of the Turnbull coefficient obtained for fcc systems are likely to be representative of close-packed crystal structures more generally. While we are unaware of any reported experimental measurements for the crystal-melt interfacial free energy of elemental Mg, the Turnbull coefficient values obtained here can be compared with measurements for the more widely studied hcp metals Zn and Cd. For these systems, data from both dihedral-angle and nucleation measurements have been used to obtained estimates of $\gamma=77$ mJ/m^2 (Ref. 53) and 87 ± 15 mJ/m^2 (Ref. 54) for Zn, and 58 mJ/m^2,[55] 59 mJ/m^2,[56] and 63 mJ/m^2 (Ref. 57) for Cd. Using lattice parameter and latent heat values from Ref. 58, these solid-liquid interfacial free energies give Turnbull coefficients in the ranges of $\alpha=0.40-0.45$ for Zn and 0.42–0.46 for Cd. The value of $\alpha=0.48$ for Mg obtained here is within 4–17% of these numbers; considering the relatively high uncertainties associated with experimental measurements of γ, this level of correspondence can be considered quite close.

In Table IV, the differences in γ between the three listed high-symmetry orientations give the following ordering of the interfacial free energies: $\gamma_{(11\bar{2}0)}>\gamma_{(10\bar{1}0)}>\gamma_{(0001)}$. Interestingly, it is found that the orientation with the lowest interfacial free energy corresponds to the close-packed crystal plane [namely, (0001)]. The same result has also been found in MD studies of fcc metals where the close-packed (111) plane is calculated to have the lowest interfacial free energy in EAM systems,[8] as well as Lennard-Jones crystals,[4,11] hard-spheres, and repulsive power-law potentials.[5] The magnitudes of the anisotropies quoted in the last two columns of Table IV are comparable to, albeit slightly smaller than those derived in previous MD studies of fcc metals. As reviewed in the introduction, CFM calculations for fcc metals yield maximum anisotropies between (111) and (100) orientations which range between 1.8 and 3.2 %; for Mg we obtain slightly smaller values for the anisotropies between (0001) and basal-plane orientations with a maximum value of 1.2%. Given that the uncertainties in the calculated Mg anisotropies are relatively high, it is not clear if this result indicating slightly smaller anisotropies for hcp Mg relative to fcc metals is meaningful. Further work is warranted to investigate this possible trend in more detail.

Experimentally, the anisotropy of solid-liquid interfacial free energies in hcp metals has been investigated for alloys of Mg,[59] as well as Cd and Zn (Refs. 59–63) through investigations of solid-particle shapes. For Cd and Zn, experimental observations are consistent with relatively high anisotropy, on the order of 30% between (0001) and basal-plane orientations. These high anisotropies are sufficient to lead to the observation of faceted morphologies for crystals formed from the melt. Passerone and Eustathopoulos[62,63] have in fact found that by varying composition it is possible to observe a roughening transition for solid-liquid interfaces in Zn-based alloys. In contrast to these observations for Zn and Cd, Miller and Chadwick[59] report that, in Mg alloys, the solid-liquid interfacial free energy is highly isotropic, based on experimental measurements of the equilibrium shapes of small liquid droplets entrained within solid grains. The present calculations for Mg yield anisotropies on the order of only a percent and are thus consistent with these early experiments. More detailed comparisons between the presently calculated γ anisotropies and experiment can be made on the basis of the observed dendrite growth directions in Mg alloys, as described in the remainder of this section.

Alloy dendrite growth is controlled by the balance of solute diffusion and capillary forces. While the former tends to make the interface morphologically unstable, the latter have the opposite effect. The anisotropy of γ generally determines both the growth directions and growth rates of dendrites, and it enters the diffusion-controlled growth problem through the local equilibrium Gibbs-Thomson relation

$$T = T_M + mC_L - \frac{T_M}{L}\sum_{i=1}^{2}\left(\gamma(\hat{n}) + \frac{\partial^2\gamma(\hat{n})}{\partial\theta_i^2}\right)\frac{1}{R_i}, \qquad (10)$$

which is written here for simplicity for a dilute binary alloy, where T is the interface temperature, T_M is the melting temperature, C_L is the solute concentration on the liquid side of the interface, m is the liquidus slope, L is the latent heat of melting, θ_i are the local angles between the normal direction $\hat{n}$ and the two local principal directions on the solid-liquid interface, and R_i are the principal radii of curvature. The interface stiffness $\gamma+\gamma''$ that enters the Gibbs-Thomson relation is a scalar in two dimensions but becomes a tensor in three dimensions: in the neighborhood of a point P on the interface, $\hat{n}$ can be specified by giving two angles φ_1 and φ_2, which are the deviations of this normal from the normal at P in the directions of two tangent orthonormal vectors $\hat{t}_1$and $\hat{t}_2$, contained in the plane perpendicular to the normal at P. The stiffness tensor is then defined by

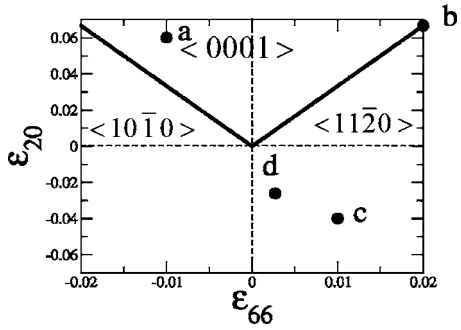

FIG. 8. Dendrite growth direction selection map based on the minimum trace of the interface stiffness tensor in the plane where ϵ_{20} and ϵ_{66} are the coefficients of the hexagonal harmonics y_{20} and y_{66}. Angular plots of the inverse of this trace corresponding to points (a)–(d) above are shown in Fig. 9.

$$S_{ij} = \left(\gamma \delta_{ij} + \frac{\partial^2 \gamma}{\partial \varphi_i \partial \varphi_j} \right). \tag{11}$$

This tensor is diagonal when $\hat{t}_1$ and $\hat{t}_2$ coincide with the principal directions on the interface at P, in which case ϕ_1 and ϕ_2 coincide with θ_1 and θ_2, and the contraction of the stiffness tensor and the tensor of curvature enters the Gibbs-Thomson relation (10). Therefore, the determination of the dendrite growth direction generally requires a full self-consistent solution of the diffusion-controlled growth problem to determine simultaneously the dendrite tip morphology and growth rate, either through the application of solvability theory[64–66] or using phase-field simulations.[67,68] However, an approximate prediction of preferred dendrite growth directions can be obtained by assuming that these directions coincide with minima of the trace of the stiffness tensor TrS $\equiv S_{11}+S_{22}$, which are directions along which capillary forces are least effective at smoothing out spherical protrusions of the interface. Expressed in terms of spherical-coordinate angles, this trace is given by

$$\mathrm{Tr}S = 2\gamma + \frac{\partial^2 \gamma}{\partial \theta^2} + \frac{1}{\sin^2 \theta} \frac{\partial^2 \gamma}{\partial \phi^2} + \cot \theta \frac{\partial \gamma}{\partial \theta}. \tag{12}$$

Guided by the MD data, which shows that the anisotropy of γ is dominated by $y_{20}(\theta, \phi)$ and $y_{66}(\theta, \phi)$, we have used Eqs. (4) and (12) to compute the directions that correspond to minima of TrS, or equivalently maxima of $1/(\mathrm{Tr}S)$, in the two-dimensional parameter space $(\epsilon_{66}, \epsilon_{20})$. The resulting dendrite growth direction selection map is shown in Fig. 8 and plots of $1/(\mathrm{Tr}S)$ as a function of spherical-coordinate angles are shown in Fig. 9, where bumps in these plots correspond to possible dendrite growth directions.

Growth directions in the basal plane, either $\langle 11\bar{2}0 \rangle$ or $\langle 10\bar{1}0 \rangle$ directions depending on whether ϵ_{66} is positive or negative, correspond to absolute minima of TrS below the solid lines in Fig. 8, and $\langle 0001 \rangle$ directions correspond to absolute minima of TrS above these lines. On these lines, which can be found analytically to be given by $\epsilon 20 = 10|\epsilon 66|/3$, $\langle 0001 \rangle$ and basal plane directions have equal minima of TrS. The MD data of Table IV clearly fall into a region where $\langle 11\bar{2}0 \rangle$ dendrites should form. This prediction is in fact in agreement with experimental observations in a number of Mg alloy systems[69,70] which have reported observing dendrites growing with basal-plane orientations with $\langle 11\bar{2}0 \rangle$ tip orientations. It is also interesting to note that for some Mg-alloy systems, off-axis dendrite growth directions such as $\langle 22\bar{4}5 \rangle$ have been reported.[69,70] As will be discussed in more detail in a future publication, the inclusion of a small component of the hexagonal harmonic y_{40} turns out to be sufficient to produce minima of TrS at these off-axis directions. It is therefore possible that solute additions increase the magnitude of ϵ_{40} so as to select these additional growth directions.

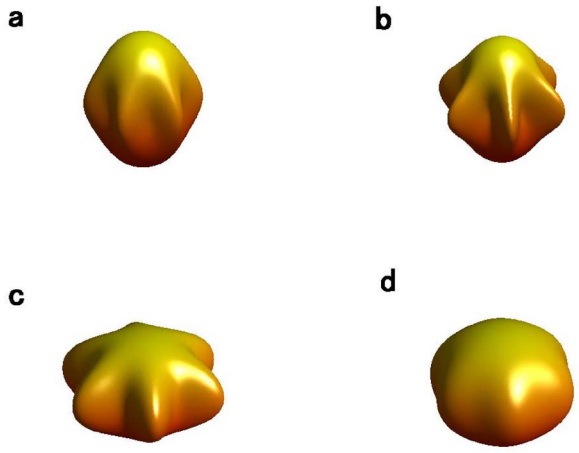

FIG. 9. (Color online) Plots of $1/(\mathrm{Tr}S)$ as a function of the spherical-coordinate angles illustrating preferred growth directions in different regions of the (ϵ_1, ϵ_2) plane: (a) $\epsilon_{20}=0.06$, $\epsilon_{66}=-0.01$; (b) $\epsilon_{20}=(10/3)*0.02$, $\epsilon_{66}=0.02$; (c) $\epsilon_{20}=-0.04$, $\epsilon_{66}=0.01$; (d) $\epsilon_{20}=-0.026$, $\epsilon_{66}=0.0027$, which corresponds to the MD data of Table IV.

VI. SUMMARY

The present work represents the initial application of the CFM to the calculation of anisotropic crystal-melt interfacial free energies for an hcp crystal. It is described how the CFM, which has previously been applied to studies of fcc and bcc systems only, can be extended to noncubic solids by making use of an expansion of $\gamma(\hat{n})$ in terms of spherical harmonics compatible with the crystal point-group symmetry. This initial application of the CFM to hcp solids has focussed on elemental Mg. For this application we developed a new EAM interatomic potential fit to crystal and liquid properties, following the earlier work of Liu *et al.*[35] Compared to this earlier potential, the current one has improved melting properties and corrects the unanticipated high-temperature stability of the bcc phase. CFM calculations based on this new

TABLE V. Parametrization of the potential functions representing the currently developed EAM potential for Mg, where energy and distance are given in units of eV and Å, respectively.

Function	Value	Cutoffs
$\phi(r)$	$(2073.5651906182/r)$	
	$\times[0.1818\exp(-22.115115867102\cdot r)$	
	$+0.5099\exp(-6.5122105254908r)$	
	$+0.2802\exp(-2.7844313071423r)$	
	$+0.02817\exp(-1.3932522996274r)]$	0–1.6
	$+\exp(13.795119773576-14.238449227620r$	1.6–2.6
	$+5.8113719144770r^2-0.92541810687079r^3)$	
	$-4.0533531215168(3.7-r)^4$	
	$+6.9691501349841(3.7-r)^5$	
	$-6.6468685095783(3.7-r)^6$	
	$+2.1727482243326(3.7-r)^7$	2.6–3.7
	$-0.12374960403430(3.7-r)^8$	
	$-1.0210685145201(6.0-r)^4$	
	$-0.81665230208338(6.0-r)^5$	
	$-1.0553724438859(6.0-r)^6$	
	$-0.34513757618316(6.0-r)^7$	2.6–6.0
	$-0.055196787794434(6.0-r)^8$	
	$+0.17225753251414(7.5-r)^4$	
	$-0.525953005713810(7.5-r)^5$	
	$+0.60129012186016(7.5-r)^6$	
	$-0.29986451887671(7.5-r)^7$	2.6–7.5
	$+0.055188968432433(7.5-r)^8$	
$\psi(r)$	$0.00019838398686504(2.7-r)^4$	0–2.7
	$+0.10046581263528(2.8-r)^4$	0–2.8
	$+0.10054028073177(2.9-r)^4$	0–2.9
	$+0.099096119019299(3.0-r)^4$	0–3.0
	$+0.090021476664876(3.3-r)^4$	0–3.3
	$+0.0068621909217769(3.8-r)^4$	0–3.8
	$+0.012393768072070(4.7-r)^4$	0–4.7
	$-0.0047476810373812(5.3-r)^4$	0–5.3
	$+0.0012360476552220(6.2-r)^4$	0–6.2
	$+0.0006214149488021(7.5-r)^4$	0–7.5
$F(\rho)$	$-\rho^{1/2}-0.21928786648389\rho^{3/2}$	
	$+0.031798479913244\rho^2$	

potential yield a Turnbull coefficient of $\alpha=0.48$ which is compatible with values derived in previous work for fcc-based EAM metals. Amongst the three high-symmetry interface orientations (0001), $(10\bar{1}0)$, and $(1\bar{2}10)$, the lowest interfacial free energy is obtained for the close packed (0001) plane, analogous to the findings in previous calculations for fcc systems which yield the lowest value of γ for the close-packed (111) orientation. The maximum anisotropy in γ between the high-symmetry orientations considered in this work is $1.2\pm0.7\%$. Finally, the experimental observations of $\langle 10\bar{1}0\rangle$ dendrites in the basal plane in Mg alloys agrees well with the fact the absolute minima of the trace of the stiffness tensor coincide with these growth directions for the MD anisotropy data. Accounting for other observed growth directions off crystal axes in these alloys requires the extension of this work to include solute effects.

ACKNOWLEDGMENTS

This research was supported by the National Science Foundation of China, the Shanghai Municipal Education Commission and Shanghai Education Development Foundation (DYS); the U. S. Department of Energy, Office of Basic Energy Sciences, under Contract Nos. DE-FG02-01ER45910 (C.A.B., M.A., and J.J.H.), DE-FG02-99ER45797 (M.I.M., K.K., and D.J.S.), and DE-FG02-92ER45471 (T.H. and A.K.) as well as the DOE Computational Materials Science Network program. The Ames Laboratory is operated by the U. S. Department of Energy (DOE) by Iowa State University under Contract No. W-7405-ENG-82. Sandia is a multiprogram laboratory operated by Sandia Corporation, a Lockheed Martin Company, for the DOE's National Nuclear Security Administration under Contract No. DE-AC04-94AL85000. Use was made of resources at the National Energy Research Scientific Computing Center, which is supported by the Office of Science of the Department of Energy under Contract No. DE-AC03-76SF00098.

APPENDIX

The interatomic potential for Mg developed in the present work is of the embedded-atom-method (EAM) form in which the total potential energy (U) is divided into two contributions, a pairwise part and a many-body embedding part:

$$U=\sum_{i=1}^{N-1}\sum_{j=i+1}^{N}\phi(r_{ij})+\sum_{i=1}^{N}F(\rho_i), \tag{A1}$$

where the subscripts i and j label distinct atoms, N is the number of atoms in the system, r_{ij} is the mean separation between atoms i and j and

$$\rho_i=\sum_{j\neq i}\psi(r_{ij}). \tag{A2}$$

Table V presents the parametrization of the three functions representing the Mg EAM potential developed in the current work. Details concerning the form of the parameterization of the potential functions can be found in Ref. 48.

[1] W. J. Boettinger, J. A. Warren, C. Beckermann, and A. Karma, Annu. Rev. Mater. Res. **32**, 163 (2002).
[2] J. Q. Broughton and G. H. Gilmer, J. Chem. Phys. **84**, 5759 (1986).
[3] R. L. Davidchack and B. B. Laird, Phys. Rev. Lett. **85**, 4751 (2000).
[4] R. L. Davidchack and B. B. Laird, J. Chem. Phys. **118**, 7651 (2003).
[5] R. L. Davidchack and B. B. Laird, Phys. Rev. Lett. **94**, 086102 (2005).
[6] J. J. Hoyt, M. Asta, and A. Karma, Phys. Rev. Lett. **86**, 5530 (2001).
[7] J. J. Hoyt and M. Asta, Phys. Rev. B **65**, 214106 (2002).
[8] J. J. Hoyt, M. Asta, and A. Karma, Mater. Sci. Eng., R. **41**, 121 (2003).
[9] J. J. Hoyt, M. Asta, and D. Y. Sun, Philos. Mag. (to be published).
[10] J. R. Morris, Phys. Rev. B **66**, 144104 (2002).
[11] J. R. Morris and X. Y. Song, J. Chem. Phys. **119**, 3920 (2003).
[12] J. R. Morris, M. I. Mendelev, and D. J. Srolovitz, J. Non-Crystalline Solids (to be published).
[13] D. Y. Sun, M. Asta, J. J. Hoyt, M. I. Mendelev, and D. J. Srolovitz, Phys. Rev. B **69**, 020102(R) (2004).
[14] Y. Mu, A. Houk, and X. Y. Song, J. Phys. Chem. **109**, 6500 (2005).
[15] M. Asta, J. J. Hoyt, and A. Karma, Phys. Rev. B **66**, 100101(R) (2002).
[16] M. S. Daw and M. I. Baskes, Phys. Rev. Lett. **50**, 1285 (1983); Phys. Rev. B **29**, 6443 (1984).
[17] D. Turnbull, J. Appl. Phys. **21**, 1022 (1950).
[18] B. B. Laird, J. Chem. Phys. **115**, 2887 (2001).
[19] G. Ghosh, Mater. Sci. Eng., A **189**, 277 (1994).
[20] T. Volkmann, W. Löser, and D. M. Herlach, Metall. Mater. Trans. A **28**, 453 (1997).
[21] A. Zambon, B. Badan, K. Eckler, F. Gärtner, A. F. Norman, A. L. Greer, D. M. Herlach, and E. Ramous, Acta Mater. **46**, 4657 (1998).
[22] M. Li, Z. Lin, G. Song, G. Yang, and Y. Zhou, Mater. Sci. Eng., A **268**, 90 (1999).
[23] D. M. Herlach, J. Phys.: Condens. Matter **13**, 7737 (2001).
[24] A. L. Greer and I. T. Walker, J. Non-Cryst. Solids **317**, 78 (2003).
[25] C. Notthoff, B. Feuerbacher, H. Franz, D. M. Herlach, and D. Holland-Moritz, Phys. Rev. Lett. **86**, 1038 (2001).
[26] S. Auer and D. Frenkel, J. Phys. A **14**, 7667 (2002).
[27] F. Spaepen, Acta Metall. **23**, 729 (1975).
[28] F. Spaepen and R. B. Meyer, Scr. Metall. **10**, 257 (1976).
[29] C. V. Thompson, Ph.D. thesis, Harvard University, Cambridge, MA, 1979.
[30] S. Liu, R. E. Napolitano, and R. Trivedi, Acta Mater. **49**, 4271 (2001).
[31] R. E. Napolitano, S. Liu, and R. Trivedi, Interface Sci. **10**, 217 (2002).
[32] R. E. Napolitano and S. Liu, Phys. Rev. B **70**, 214103 (2004).
[33] M. E. Glicksman and N. B. Singh, J. Cryst. Growth **98**, 277 (1989).
[34] M. Muschol, D. Liu, and H. Z. Cummins, Phys. Rev. A **46**, 1038 (1992).
[35] X. -Y. Liu, J. B. Adams, F. Ercolessi, and J. A. Moriarty, MSMSE **4**, 293 (1996).
[36] M. Buerger, *Elementary Crystallography: An Introduction of the Fundamental Geometric Features of Crystals* (MIT Press, Cambridge, 1978).
[37] M. Kara and K. Kurki-Suonio, Acta Crystallogr., Sect. A: Cryst. Phys., Diffr., Theor. Gen. Crystallogr. **37**, 201 (1981).
[38] J. D. Althoff, P. B. Allen, R. M. Wentzcovitch, and J. A. Moriarty, Phys. Rev. B **48**, 13253 (1993).
[39] J. A. Moriarty and J. D. Althoff, Phys. Rev. B **51**, 5609 (1995).
[40] A. E. Carlsson, Solid State Phys. **43**, 1 (1990).
[41] F. Ercolessi and J. B. Adams, Europhys. Lett. **26**, 583 (1994).
[42] P. G. Shewmon, Trans. Am. Inst. Min., Metall. Pet. Eng. **206**, 918 (1956).
[43] G. T. Murray and T. A. Lograsso, *Metals Handbook*, 10th ed. (ASM International, Materials Park, OH, 1990), Vol. 2, p. 1133.
[44] A. I. Efimov, L. P. Belorukova, I. V. Vasilkova, and V. P. Chechev, *Svoistva Neorganicheskih Soedinenii* (Himiia, Leningrad, 1983) (in Russian).
[45] B. G. Lifshitz, V. S. Kraposhin, and Ya. L. Linetskaia, *Fizicheskie Svoistva Metallov i Splavov* (Metallurgia, Moscow, 1980) (in Russian).
[46] Y. Waseda, *The Structure of Non-crystalline Materials* (McGraw-Hill, New York, 1980).
[47] J. R. Morris, C. Z. Wang, K. M. Ho, and C. T. Chan, Phys. Rev. B **49**, 3109 (1994).
[48] M. I. Mendelev, S. Han, D. J. Srolovitz, G. J. Ackland, D. Y. Sun, and M. Asta, Philos. Mag. **83**, 3977 (2003).
[49] J. B. Sturgeon and B. B. Laird, Phys. Rev. B **62**, 14720 (2000).
[50] J. H. Rose, J. R. Smith, F. Guinea, and J. Ferrante, Phys. Rev. B **29**, 2963 (1984).
[51] S. Baroni, A. Dal Corso, S. de Gironcoli, P. Giannozzi, C. Cavazzoni, G. Ballabio, S. Scandolo, G. Chiarotti, P. Focher, A. Pasquarello, K. Laasonen, A. Trave, R. Car, N. Marzari, and A. Kokalj, http://www.pwscf.org/
[52] J. P. Perdew, K. Burke, and M. Ernzerhof, Phys. Rev. Lett. **77**, 3865 (1996).
[53] D. W. G. White, Trans. Metall. Soc. AIME **236**, 796 (1966).
[54] A. Passerone, R. Sangiori, N. Eustathopoulos, and P. Desre, Met. Sci. **13**, 359 (1979).
[55] K. F. Kelton, Solid State Phys. **45**, 75 (1991).
[56] D. W. G. White, Metall. Trans. **3**, 1933 (1972).
[57] H. Jones, Mater. Lett. **236**, 796 (1966).
[58] *Smithells Metals Reference Book* (Elsevier Butterworth-Heinemann, Burlington, MA, 2004).
[59] W. A. Miller and G. A. Chadwick, Proc. R. Soc. London, Ser. A **312**, 257 (1969).
[60] B. Mutaftschiev and J. Zell, Surf. Sci. **12**, 317 (1968).
[61] J. W. Cahn, W. B. Hillig, and G. W. Sears, Acta Metall. **12**, 1421 (1964).
[62] A. Passerone and N. Eustathopoulos, J. Cryst. Growth **49**, 757 (1980).
[63] A. Passerone and N. Eustathopoulos, Acta Metall. **30**, 1349 (1982).
[64] D. A. Kessler and H. Levine, Acta Metall. **36**, 2693 (1988).
[65] A. Barbieri and J. S. Langer, Phys. Rev. A **39**, 5314 (1989).
[66] M. Ben Amar and E. Brener, Phys. Rev. Lett. **71**, 589 (1993).
[67] A. Karma and W. J. Rappel, Phys. Rev. E **53**, R3017 (1996). **57**, 4323 (1998).
[68] N. Provatas, N. Goldenfeld, and J. Dantzig, Phys. Rev. Lett. **80**, 3308 (1998).
[69] K. Pettersen and M. Ryum, Metall. Trans. A **20**, 847 (1989).
[70] K. Pettersen, O. Lohne, and N. Ryum, Metall. Trans. A **21**, 221 (1990).